Characterization of the 3-D microstructure of mango (*Mangifera indica* L. *cv. Carabao*) during ripening using X-ray computed microtomography

Dennis Cantre, Els Herremans, Pieter Verboven, Jerry Ampofo-Asiama, Bart M. Nicolaï

PII: S1466-8564(13)00206-3
DOI: doi: 10.1016/j.ifset.2013.12.008
Reference: INNFOO 1111

To appear in: *Innovative Food Science and Emerging Technologies*

Received date: 29 September 2013
Accepted date: 15 December 2013

Please cite this article as: Cantre, D., Herremans, E., Verboven, P., Ampofo-Asiama, J. & Nicolaï, B.M., Characterization of the 3-D microstructure of mango (*Mangifera indica* L. *cv. Carabao*) during ripening using X-ray computed microtomography, *Innovative Food Science and Emerging Technologies* (2013), doi: 10.1016/j.ifset.2013.12.008

Characterization of the 3-D microstructure of mango (*Mangifera indica* L. *cv. Carabao*) during ripening using X-ray computed microtomography

Dennis Cantre[1], Els Herremans[1] Pieter Verboven[1], Jerry Ampofo-Asiama[1], Bart M. Nicolaï[1, 2]

[1]BIOSYST-MeBioS, KU Leuven, Willem de Croylaan 42, B-3001 Leuven, Belgium

[2]Flanders Centre of Postharvest Technology, Willem de Croylaan 42, B-3001 Leuven, Belgium

Corresponding author:

Bart M. Nicolaï, Flanders Centre of Postharvest Technology / BIOSYST-MeBioS, KU Leuven, Willem de Croylaan 42, B-3001 Leuven, Belgium

Tel.: +32 16 32 23 75; Fax: +32 16 32 29 55; e-mail: bart.nicolai@biw.kuleuven.be

Keywords: mango, ripening, microstructure, X-ray computed microtomography

Submitted to: Innovative Food Science and Emerging Technologies

Version: 2nd

Abstract

In this study, X-ray computed microtomography (X-ray μCT) was applied to investigate the changes in 3-D microstructure of mango during ripening at 20°C. X-ray μCT provided a unique insight of the undamaged tissue and pore network during ripening. Analysis of the pore and tissue network revealed differences in the microstructure along the radial axis of the fruit and microstructural changes during ripening. Multivariate statistical analysis unveiled that ripening was associated with a decrease in pore size, and increase in pore fragmentation and pore specific surface area. These structural parameters have the highest discriminating ability, correctly classifying unripe from ripe fruit samples. The study concludes that ripening can be successfully characterized on the basis of its 3-D microstructure using X-ray microtomography.

Industrial relevance

This study identified important parameters to describe the ripening process on the basis of microstructure. As today microtomography technology allows for scanning only a small tissue sample from the fruit, the pace at which tomography technology is advancing will allow for scanning whole fruit with sufficient resolution and without any need for sample preparation. Results from this study could be applied for non-destructive determination of fruit microstructure for assessing fruit quality in relation to the ripening process.

Highlights

- First report on 3-D microstructural changes of mango during ripening
- Automatic segmentation can be applied to measure and visualize mesocarp cells
- Significant changes in microstructure were observed during ripening

1 Introduction

Mango ripening is a part of its natural senescence, wherein an irreversible degradation of organelles, changes in chemical constituents, flavor and texture occur (Brecht & Yahia, 2009). As most climacteric fruit, mango ripening is regulated by ethylene. Ethylene functions by coordinating the expression of thousands of genes responsible for changes in color, texture and taste of the fruit (Singh, Singh, Sane, & Nath, 2013). During ripening, mango changes color from green to reddish orange or yellow. The change in color is attributed to disappearance of chlorophyll and increase in amount of other pigments including anthocyanins and carotenes (Grierson, Tucker, & Robertson, 1981; Lizada, 1993; Parikh, Nair, & Modi, 1990; Singh et al., 2013). Pulp firmness change is another important quality factor that not only affects consumer acceptance but also susceptibility to bruising and compression resistance during transportation and handling. The loss in firmness during ripening has been attributed to changes in cell wall and pectic substances in the middle lamella (Selvaraj, Kumar, & Pal, 1989; Brecht & Yahia, 2009). Changes in cell wall composition and structure will also affect the arrangement of cells in the tissue (Abera et al., 2013) and thus firmness and texture perception of the fruit, but this has received little or no attention with respect to mango ripening.

Han, Tian, Meng, & Ding (2006) evaluated the microstructure of 'Red 6' mangoes during ripening using transmission electron microscope and light microscopy. They observed that cell walls separated from tri-cellular junctions during early stages of ripening followed by swelling of the cell wall at the latter stage of ripening. However, although light microscopy and transmission electron microscopy provide useful information, they are limited to destructive analysis of thin 2-D sections. Measurements made from these 2-D sections are highly dependent on the section

plane and do not reflect the true measurements based on the whole volume (e.g., Feret length and width). Thus, measurements made from the 2-D sections yield information that is not useful for determining the 3-D structure. Ultimately, the relation of the 3-D structure to the mechanical and transport properties of fruit, cannot be deduced using 2-D images (Herremans et al., 2013; Ho et al., 2013a). The importance of 3-D microstructure in fruit with regards to texture and mechanical properties has also been described by Mebatsion, Verboven, Ho, Verlinden, & Nicolai (2008) and Abera et al. (2013), amongst others, while its effect on gas transport was studied by Ho et al. (2009, 2011, 2013a,b,c).

Determination and measurement of the intact tissue and pore network was made possible through the use of X-ray µCT. It was also used to visualize gas-filled intercellular spaces during storage of cucumber (Kuroki, Oshita, Sotome, Kawagoe, & Seo, 2004). Mendoza et al. (2007) characterized the pore network of apple in its intact state using a laboratory based CT system. Verboven et al. (2008) further used synchrotron X-ray CT to characterize the gas exchanged pathways in pome fruit. X-ray µCT was also used to characterize microstructural changes during the development of browning in 'Braeburn' apples (Herremans et al., 2013).

Thus, while studies have been performed to elucidate the phenomenon of mango ripening, its relation to microstructure, especially to the 3-dimensional cell and tissue structural properties is not known. This study aims to provide an insight on how the 3-D microstructure of mango changes during the ripening process when the fruit transforms from a mature to table ripe stage. This was accomplished through the use of X-ray microtomography of tissue *in vivo* obtained at different stages during ripening of the fruit, three-dimensional image processing and multivariate statistics.

2 Materials and methods

2.1 Mango fruit and treatments

Mangoes (cv. 'Carabao') were obtained from a commercial farm in Cebu, Philippines, during the month of September 2012. Mangoes were optimally picked at their full maturity characterized by full raised shoulders at the end stem but remaining firm (Mohammed & Brecht, 2002). In addition, fruit harvested were fully green and free of disease. Sample preparation was in accordance to industry standards for export as outlined in Yaptenco, Lacao, Esguerra and Serrano (2010). Fruit were selected for weight, in the range of 270 - 350 g and subjected to hot water treatment at 55°C for 5 minutes. The fruit were then air dried and packed in corrugated carton boxes with each box containing 12 kg. The boxes were transported by airfreight to KU Leuven, Belgium. Transit time from the Philippines to the laboratory was approximately 3 days. The temperature of the mangoes was maintained at 13°C during transit. The mangoes were ripened at 20°C with a relative humidity of 55 ± 5% for up to 9 days. Color measurements were monitored with a Minolta colorimeter CR-300 (Minolta Corp., Ramsey, NJ, U.S.A.). Microstructure analysis was done at three days interval.

2.2 X-ray computed microtomography

Prior to scanning by means of X-ray CT, mangoes were equilibrated to room temperature overnight. Cylindrical samples (Figure 1) measuring 5.5 mm in diameter and 5 mm in height were obtained from the outer mesocarp ($x > R$-5 mm, with R, the radius of the fruit on the equator) and inner mesocarp (R-5 mm $\geq x > 0.3R$) on the equatorial positions of the sunny and shade side of the fruit. Thus, for every fruit, 4 samples were measured. Subsequently, the

samples were wrapped in parafilm and packed in polystyrene foam to prevent dehydration that might cause undesirable motion artefacts in the subsequent CT scan (Herremans et al., 2013). The procedure was repeated for 6 fruit stored at 20°C for 4 distinct storage durations. Damaged tissue samples due to sample preparation were virtually cropped prior to analysis. This includes cropping of the sides (1 mm) and the top and bottom portion (1.25 mm) of the sample to ensure intact and undamaged samples for analysis (Figure 1c). The final volume left for analysis was 24 mm^3.

A Skyscan 1172 (Bruker microCT, Kontich, Belgium) was used to obtain multiple X-ray shadow projections from multiple angular views as the object rotates on a high precision stage. Preliminary trials were done to determine optimum CT scanning parameters that yield good contrast for image segmentation and thresholding. Repeatability, resolution and scanning time were also considered. From the trials (data not shown), it was found that an operating voltage of 60 kV with a current of 167 µA renders an image with sufficient contrast, using a rotation step of 0.4° and a rotation angle of 180°. Frame averaging was set to a modest value of 3 with exposure time of 295 ms and the size of the image set at 2000 × 1048 pixels. Pixel resolution of the image was set at 4.8 µm. Scanning time was 20 minutes to obtain 511 projections, using the above mentioned conditions.

Feldkamp's algorithm (Feldkamp, Davis, & Kress, 1984) was implemented using NRecon 1.6.5.8 software (http://www.skyscan.be/next/downloads.htm) to reconstruct cross-section images ('slices') from the cone-beam X-ray shadow projections. Reconstruction parameters were also optimized to obtain good segmentation results, yielding high contrast, low noise images. For these reasons, smoothing was set to a modest value of 2 to minimize noise. Consequently, beam hardening correction and ring artefact reduction were set at 35% and 10 respectively. The linear

attenuation range (dynamic range) was set at 0 to 0.122 to improve contrast and standardize the grayscale range of the output images. The output file type was an 8-bit bitmap image. Reconstruction took about 17 minutes for 937 cross-section images or a speed of about 1.1 s per slice.

2.3 Image processing

To facilitate segmentation, a global threshold was defined to separate air spaces (low X-ray attenuation, resulting in lower grayscale intensity) and cells (high X-ray attenuation, rendering high grayscale values). The global threshold value defines the grayscale limit. Above this limit, the pixel was considered as tissue or water filled void, and below it was considered as gas-filled intercellular space. In a bimodal grayscale histogram, the global threshold value can simply be chosen as the deep valley separating the air and cell peak while in a unimodal histogram, where there is no clear peak separation, analyzing the statistics of the histogram can be applied. To optimize the threshold value, Otsu's algorithm for segmentation was used. The algorithm is based on discriminant analysis and maximizes the 'between-class variance' of the grayscale histogram to give the best separation into background and object classes (Gonzales-Barron & Butler, 2006).

Segmentation procedures were performed using Image J 1.47n (National Institutes of Health, USA), CTAn 1.12 (Bruker microCT, Kontich, Belgium) and Avizo 7 (VSG, France). Morphometric parameters (Table 1) as described by Herremans et al. (2013) were determined after removing noise and pores smaller than the detection limit of 3.13×10^{-6} mm^3, equivalent to 27 voxel volume. Morphometric parameters were calculated using Image J 1.47n (National

Institutes of Health, USA), CTAn 1.12 (Bruker microCT, Kontich, Belgium) and Avizo 7 (VSG, France).

Automatic segmentation of individual cells was not possible due to the insufficient contrast between cytoplasm and cell wall. Hence, this was done manually using the interpolation and wrapping method, enfolding the selected pixels in 3-D to create cell volumes. Also, an attempt was made to automatically segment individual cells using the watershed segmentation method of Meyer and Beucher (1990). The procedure starts with binarization of the grayscale image and filling of unnecessary holes. The filling of holes is required as separation by watershed is based on a distance map which is sensitive to these small holes. A distance map was then created, giving each pixel a value based on their distance from the black background. From the distance map, a regional maxima was identified by subtracting a contrast factor. The identified regional maxima was labeled as markers. These markers served as the seed for the flooding. The markers were filled like a drop of water falling towards the nearest minimum until the catchment basin is filled to a certain depth. The crest lines separating the markers were identified as the watershed lines. The separated cells were produced from the logical difference between the watershed line and the initial binarized image. Incorrectly separated cells and unseparated cluster of cells were virtually filtered using previous knowledge of cell shape and size obtained from manual segmentation. The method was implemented in Avizo 7 (VSG, France).

2.4 Representative elementary volume analysis

To ensure that the sample is large enough to provide representative properties of the tissue, representative elementary volume analysis using the method of Mendoza et al. (2007) was performed. Representative elementary volume is defined as the range of volumes over which a

statistical average can be performed (Bear, 1972). In this paper, the effect on calculated tissue porosity (total volume of segmented air spaces over total volume of the sample) of six volume sizes extracted from the same stack of images was analyzed. Images were analyzed in triplicates using four different mangoes (n=12/volume size). The procedure was implemented using CTAn 1.12 (Bruker microCT, Kontich, Belgium). Six different volumes were generated by varying the cube length to 32, 64, 128, 256, 320, and 512 pixels (4.87 µm/pixel). The average porosity with standard deviation for each volume sizes was calculated. Sensitivity analysis was performed to study how elementary volume and porosity changes with respect to changes in the threshold value. Relative sensitivity was determined after increasing and decreasing the threshold by 10%. Relative sensitivity was calculated using the method of Abera et al. (2013).

2.5 Statistical analysis

Results of the quality measurements and morphometric analysis were subjected to analysis of variance using the PROC GLM procedure in SAS Enterprise software version 4.3 (SAS Institute, Cary, NC, USA). Morphometric analysis data were also subjected to Partial least square regression for discriminant analysis (PLS-DA) using the nonlinear iterative partial least square (NIPALS) algorithm. PLS-DA was implemented in Unscrambler software version 10.1 (CAMO Software, Oslo, Norway). Prior to multivariate analysis, the data was standardized by dividing by its standard deviation then a full cross validation PLS-DA was performed.

3 Results

3.1 Image segmentation

Segmentation of the X-ray images was performed to separate the tissue and the gas-filled intercellular spaces. Segmentation was needed before any calculation on the tissue volume could be made. The grayscale image of a typical CT cross-section of unripe mango (Figure 2a) showed enough contrast to differentiate between the dark background, recognized as the pores and the light objects, recognized as the tissue. Unlike a bimodal histogram where the threshold can simply be placed at the local minima separating the pore peak and the tissue peak, the resulting histogram was unimodal, characterized by absence of clear peak separation and usually appearing in images where a less populated class belongs to a tail in the histogram. In the case of mango, pore space was generally small and this less populated class appeared at the front tail of the histogram (Figure 2d) without any clear separation between the pore and tissue peak. A global threshold value was selected based on the application of Otsu's algorithm to the unripe sample (Figure 2b) and was verified manually. The grayscale intensity histogram (Figure 2d) shows the obtained global threshold value of 63. The global threshold allowed separation of the tissue and pores in the image. The peak observed at a grayscale value of zero, was due to limiting the dynamic range from 0 to 0.122. This transformed the pixels with linear attenuation below zero (generally due to noise) to zero.

3.2 Representative elementary volume analysis

Representative elementary volume analysis (Figure 3a) shows the porosity values for different sizes of a sample from 4 different fruit. The result indicates no significant difference in the mean of porosities obtained from the different sizes. However, a general decrease in the confidence interval was observed as volume size was increased. This is primarily due to the averaging of sampling errors in large volume sizes. Analysis of standard deviation (Figure 3b) for each

volume size revealed that as volume size increases the standard deviation generally decreased. In addition, it was observed that for volume sizes of 0.62 × 0.62 × 0.62 mm or larger, there is no appreciable change in the standard deviation. The results thus suggest that a volume of 0.242 mm^3 can be considered as an elementary volume for subsequent quantitative analysis. Sensitivity analysis showed no change in the elementary volume obtained as the grayscale threshold was increased or decreased by 10% (data not shown). This suggests that the elementary volume is not affected by slight changes in the threshold value. Porosity, however, showed an increase of 0.83 % when the threshold was increased by 10%. It also showed a decreased of 26% when the threshold was decreased by 10 %. For comparison, the porosity decreased by 31.7 % and 37.2 % in the inner and outer mesocarp respectively during ripening.

3.3 3-D structural parameters of mesocarp cells

In vivo morphometric analysis of cells derived from manual segmentation (Figure 4) showed an increase in cell volume along the fruit radius (Table 2). A cubic millimeter of tissue contains on the average 761 cells for outer mesocarp and 1109 cells for the inner mesocarp. An increase in cell surface area and a decrease in cell specific surface area along the fruit radius is also noted (Table 2). An increase in cell size was also evident from the increase in cell length and cell width along the radius of the fruit. The shape of the cells in terms of cell length to width ratio and sphericity does not significantly change along the radius. Results suggest that the increase in cell surface area and decrease in specific surface area is not brought about by the change in shape but rather on the increase in cell size along the fruit radius.

Morphometric analysis of cells obtained through automatic segmentation using the watershed algorithm (Figure 4 & Table 3) confirmed the increase in cell volume along the radial axis of the

fruit. In addition, the cell length, width, and length to width ratio is not significantly different with the cells obtained from manual thresholding. A clear distinction between the outer and inner mesocarp can also be observed from the watershed segmentation as compared to manually segmented cells. This is mainly due to the higher amount of cells sampled giving a more accurate mean with significantly less standard error. The results suggest the viability of automatic segmentation as a tool for determining morphometric parameters of cells. The advantage of less time and more accurate measurement can potentially be translated into an in-process measurement system for fresh fruits and vegetables where fast scanning and quick decision making is important.

To differentiate the unripe from the ripe condition, an attempt was made to segment mesocarp cells from a ripe fruit but this proved difficult due to the loss of pores and decrease in pore size during ripening (Figure 5). This, accompanied by the loss of cell turgor, made cell boundaries difficult to distinguish as cells were closely grouped into clusters rendering separation by manual segmentation or watershed procedure nearly impossible. Isolated cells from a ripe fruit using the automatic segmentation procedure (Figure 5 & Table 4) yielded a highly irregular shape with significantly lower sphericity than unripe mesocarp cells. While the highly irregular shape and corresponding decrease in sphericity can be attributed to loss of cell turgor, it may also be possible that cell leakage may have occurred (Figure 6). In micro-CT images, extracellular liquid cannot be distinguished from intracellular liquid as they render the same contrast in the images. However, as a result of cell leakage it is likely that the size and shape of intercellular spaces changes as well. Extracellular liquid will accumulate in the narrow voids due to capillary suction, not only reducing the number of sharp edged intercellular spaces, but also disconnecting long

and continuous pores connected by these narrow voids. The extracellular water may also have contributed to the irregular shape of the segmented cells of the micro-CT images.

3.4 Pore network analysis

A highly complicated pore network in mango fruit with a high degree of connectivity was found (Figure 7 & 8). However, not all pores were completely interconnected. Outer mesocarp pores appeared wider than inner mesocarp pores. In addition, there was an observed decrease in pore size and loss of pore connectivity during ripening. These produced a more fragmented pore structure with a higher number of narrow and isolated pores. Analysis of individual pores (Figure 9) showed varying size and shapes both in the outer and inner mesocarp. These individual pores vary in size by an order of magnitude of 3 from the detection limit of 3.13×10^{-6} mm^3 to 5.79×10^{-3} mm^3. In addition, the equivalent diameter varies from 18 µm to 223 µm. The inner mesocarp had small pores: 80% of the pores had an equivalent diameter of less than 40 µm contributing to 35-41% of the total pore volume. The outer mesocarp on the other hand had 80% of its pores with equivalent diameter less than 44 µm contributing to only 18-25% of total pore volume. About 50% of the total pore volume was comprised of pores having an equivalent diameter less than 72 µm and 44 µm for outer and inner mesocarp, respectively.

Upon ripening, structural transformation occurs in the outer mesocarp. The pores size shifted from a higher to a lower size fraction (Figure 9). While about 80% of pores on the outer mesocarp of ripe mango still have an equivalent diameter of less than 44µm, a higher volume contribution was reached, amounting to 26-38% of total pore volume compared to 18-25% for the unripe. About 50% of the total pore volume was comprised of pores having an equivalent diameter less than 56 µm, a significantly lower value compared to 72 µm for the unripe outer

mesocarp. Individual analysis of pores (Table 4) showed an increase in sphericity and number of pores during ripening. These findings go along with the decrease in sphericity of cells during ripening that suggest cell leakage (see above). This cell leakage may have separated pores that are once connected, effectively increasing the number of pores, while the pores become isolated air pockets (bubbles) in extracellular water and this can dramatically increase the pore sphericity (Table 4 & Figure 5d).

The inner mesocarp, on the other hand, showed no significant change in its pore size distribution during ripening. About 80% of its pores have an equivalent diameter less than 40 µm contributing to 35-45% of total pore volume, which is not significantly different from the unripe condition. In addition, about 50% of the total pore volume is comprised of pores having an equivalent diameter of less than 45 µm (Figure 9) which is also not significantly different as the unripe condition. There was, however, a reduction of 28% in the total number of pores, from 3346 to 2397 pores per cubic millimeter.

A general decrease in porosity (Figure 10 & Table 5) was observed with values as low as 5.3% and 9.3% detected in ripened tissues in inner and outer mesocarp, respectively. The observed increase in pore specific surface area in the outer mesocarp agrees with the results of pore size distribution, confirming the shift in pore size from a larger size fraction to a smaller size fraction. The smaller size fraction provided larger surface area per unit volume of tissue giving a higher value of pore specific surface area. The shift to smaller pore size fraction was also reflected in the decrease in pore structure thickness. Pore connectivity, pore fragmentation and Euler number on the other hand reflect the decrease in connectivity in ripened tissues, separating pores that were previously connected. Ripening process also decreased the maximal pore volume in the outer and inner mesocarp. The increase in tissue and pore anisotropy seems to indicate

preferential alignment of structures during ripening. This alignment did not form highly connected and organized structures as indicated in the decrease in pore connectivity and increase in pore fragmentation and Euler number but instead suggests a local redistribution of water during ripening. Pore space distribution statistics showed that skewness and kurtosis remained relatively unaffected. Biggest change was generally observed in the outer mesocarp of the fruit as compared to the inner mesocarp.

3.5 Partial least square - discriminant analysis

An attempt was made to use multivariate analysis to more successfully determine the complex changes in tissue microstructure and identify microstructural descriptors to help explain the ripening process. A PLS-DA bi-plot (Figure 11) showed that the first 2 latent variables explained 78 and 46% of the variance in structural parameters and response variables, respectively. Adding 3 more latent variables explained 95 and 80% of the variance. Based on these variables, the samples were classified based on their ripeness and position of tissue sample in the fruit. On the basis of ripeness, all of the 40 samples (24 unripe and 16 ripe) were correctly classified, showing a significant change in microstructure during ripening irrespective of the tissue sampling position in the fruit. On the basis of tissue sample position in the fruit, 20 inner mesocarp samples were correctly classified. However, 2 out of 20 outer mesocarp samples were misclassified. The misclassified outer mesocarp samples are both from the ripe condition. It should be noted that the ripening process in the PLS-DA bi-plot goes toward the direction of inner mesocarp. This suggests that the microstructural difference in the outer and inner mesocarp decreases during ripening. Morphometric parameter results further showed that while inner and outer mesocarp

have different initial values in maximal individual pore volume and pore fragmentation, they approach a value not significantly different from each other after ripening.

Multivariate approach using PLS-DA further identified the 3 most important variable related to ripening, namely, pore specific surface area, pore fragmentation, and pore structure thickness. These 3 parameters showed the most change during ripening, irrespective of the tissue sampling position (Figure 10 & Table 5). To discriminate between the tissue sampling position in the fruit, tissue anisotropy and pore structure thickness were found to be the most important parameters. It should be noted that tissue anisotropy and pore structure thickness showed a significantly different value for inner and outer mesocarp during ripening. Tissue anisotropy indicated a higher alignment of tissue structure in the inner mesocarp compared to the outer mesocarp while pore structure thickness further confirmed pore size distribution results of smaller pores in the inner mesocarp of fruit.

4 Discussion

The observed color change from green to yellow (data not shown) was attributed to degradation of chlorophyll during ripening (Lizada, 1993). This shift in color was also attributed to the conversion of chloroplast to chromoplast and the corresponding formation and release of carotenoids (Parikh et al., 1990). The color change were in agreement to those obtained by Hoa, Ducamf, Lebrup, and Baldwin (2002) and Hidalgo, De la Cruz, Parkin, and Garcia (1997) in ‘Kent’, ’Tommy Atkins’, ‘Lirfa’, and ‘Manila’ mangoes which suggest normal ripening of the mango samples.

With regards to the representative elementary volume, the value obtained was not affected by changing the threshold by 10%. This validates the obtained elementary volume as the minimum

volume for precise three-dimensional microstructural measurements and will help serve as a guide for future microstructure studies in mango. Porosity on the other hand was found to change with threshold and this was not surprising. As opposed to a bimodal histogram where the threshold can be placed at the local minima separating the pore and tissue peak, the observed histogram was unimodal and the threshold value was between the tail and the peak of the histogram due to the absence of clear peak separation. Thus, a change in threshold will significantly affect the porosity. As observed from sensitivity analysis, the porosity change due to a change in threshold value was lower than the observed change in porosity due to ripening. This implies a greater sensitivity of porosity to the ripening process and suggests that a change in threshold will not affect the microstructural change observed during ripening.

The ease of use of watershed procedure for fast and automatic segmentation of cells holds promise for observing cell morphologies in microstructural studies of fruits to answer valid research questions rather than non-destructive determination of fruit disorders. Herremans et al. (2013, unpublished results) successfully used the technique to isolate and segment individual apple and pear cells. Individual cell morphology including cell to cell connectivity may be an important component of texture (Volz, Harker, Hallet, & Lang, 2004). This cell isolation technique may serve as a tool for cellular network analysis to better understand the development of texture in mango.

The observed microstructural difference between inner and outer mesocarp and their different microstructural response during ripening, suggest the importance of radial distance in determining and evaluating the ripening process. Similar change in the outer mesocarp (during ripening) was observed in cucumber after harvest (Kuroki et al., 2004). Result suggests that microstructural changes during ripening tend to favor a decrease in pore size such that long and

continuous pore structures are disconnected and narrowed due to loss of cell turgidity during ripening. This change from a highly connected and complicated pore network to isolated small and narrow pores during ripening may significantly affect the gas exchange and ultimately the respiration of the fruit as described by Lammertyn et al. (2003a,b) and Ho et al. (2013a,b). Modification of cell wall polysaccharide by solubilization, de-esterification, and depolymerization (Voragen, Pilnik, Thubault, Axelos, & Renard, 1995) along with the decrease in the amount of phospholipid in the lipid bilayer (Suzuki, 1993) during ripening may induce deterioration of biomembrane function. This deterioration may have allowed leakage of intracellular substances into the gas-filled intercellular spaces. This leakage may have contributed to the decrease in sphericity of cells and increase in sphericity of pores during ripening. In addition, this cell leakage may also have increased pore specific surface area and pore fragmentation, and may have decreased pore structure thickness as shown in the plot of morphometric parameters. These parameters were also the one identified by PLS-DA as the important parameters in describing the ripening process.

5 Conclusion

This study utilized X-ray microtomography and 3-D microstructure analysis to obtain structural and morphometric parameters of mango during ripening. Result showed changes in microstructure along the radial axis of the fruit and clear changes in the microstructure during ripening. Relevant microstructural properties were identified to describe structural changes during ripening, which is seen as a decrease in porosity and loss of connectivity of the pores. To

relate these changes to changes in firmness and other quality attributes of the fruit remains to be done and will allow better understanding of the ripening process.

The study showed the general feasibility of X-ray CT analysis of the microstructure of mango fruit and thus opens possibilities for application of 3-D microstructure analysis in relation to novel and optimized storage technologies as well. Cultivar differences may exist in mango, and 3-D microstructural characterization can also be used to relate structural parameters to quality and storability of different cultivars.

6 Acknowledgements

Financial support of FWO Vlaanderen (project G.0645.13) and the University of Leuven (project OT 12/055) is gratefully acknowledged. Dennis Cantre is an IRO scholar of KU Leuven. Els Herremans is a doctoral fellow of the IWT (Flemish agency for Innovation by Science and Technology).

7 References

Abera, M.K., Solomon, W.F., Verboven, P., Ho, Q.T., Carmeleit, J., & Nicolai, B.M. (2013). Virtual fruit tissue generation based on cell growth modelling. *Food and Bioprocess Technology*, 6(4), 859-869.

Bear, J. (1972). Dynamics of fluids in porous media. New York: Dover, (Chapter 1).

Brecht, J.K., & Yahia, E.M. (2009). Postharvest physiology. In: R.E. Litz (Ed.), *The mango: botany, production and uses* (pp. 484-516). Oxfordshire, UK: CAB International.

Feldkamp, L.A., Davis, L.C., & Kress, J.W. (1984). Practical cone-beam algorithm. *Journal of the Optical Society of America*, A.1(6), 612–619.

Gonzales-Barron, U., & Butler, F. (2006). A comparison of seven thresholding techniques with the k-means clustering algorithm for measurement of bread-crumb features by digital image analysis. *Journal of Food Engineering*, 74, 268-278.

Grierson, D., Tucker, G. A., & Robertson, N. G. (1981). The molecular biology of ripening. In J. Friend (Ed.), *Biochemistry of Fruit and Vegetables* (pp.179–191). London: Academic Press.

Gunderson, H.J.G., Boyce, R.W., Nyengaard, J.R., & Odgaard, A. (1993). The Conneulor: unbiased estimation of connectivity using physical dissectors under projection. *Bone*, 14, 217-222.

Han, J., Tian, S., Meng, X., & Ding, Z. (2006). Response of physiologic metabolism and cell structures in mango fruit to exogenous methyl salicylate under low-temperature stress. *Physiologia Plantarum*, 128, 125-133.

Hahn, M., Vogel, M., Pompesius-Kempa, M., & Delling, G. (1992). Trabecular bone pattern factor – a new parameter for simple quantification of bone microarchitecture. *Bone*, 13, 327-330.

Herremans, E., Verboven, P., Bongaers, E., Estrade, P., Verlinden, B.E., Wevers, M., et al. (2013). Characterisation of 'Braeburn' browning disorder by means of X-ray micro-CT. *Postharvest Biology and Technology*, 75, 114-124.

Herremans, E., Verboven, P., Bongaers, E., Estrade, P., Verlinden, B., Wevers, M., et al. (2013, April). *Isolation of single cells and pores for the characterisation 3-D fruit tissue microstructure based on X-ray micro-CT image analysis*. Proceedings of InsideFood Symposium, Leuven, Belgium.

Hidalgo, M., De la Cruz, J., Parkin, K.L., & Garcia, H. (1997). Refrigerated storage and chilling injury development of Manila mangoes (*Mangifera indica L.*). *Acta Horticulturae*, 455, 718-725.

Hildebrand, T., & Ruegsegger, P. (1997). A new method for the model independent assessment of thickness in three dimensional images. *Journal of Microscopy*, 185, 67-75

Ho, Q.T., Verboven, P., Mebatsion, H.K., Verlinden, B.E., Vandewalle, S., & Nicolaï, B.M. (2009). Microscale mechanisms of gas exchange in fruit tissue. *New Phytologist*, 182, 163-174.

Ho, Q.T., Verboven, P., Verlinden, B., Herremans, E., Wevers, M., Carmeliet, J., et al. (2011). A 3-D multiscale model for gas exchange in fruit. *Plant Physiology*, 155(3), 1158-1168.

Ho, Q., Carmeliet, J., Datta, A., Defraeye, T., Delele, M., Herremans, E., et al. (2013a). Multiscale modeling in food engineering. *Journal of Food Engineering*, *114(3)*, 279-291.

Ho, Q., Verboven, P., Fanta, S., Abera, M., Retta, M., Herremans, E., et al. (2013b). A multiphase pore scale network model of gas exchange in apple fruit. *Food and Bioprocess Technology*, doi:10.1007/s11947-012-1043-y

Ho, Q., Verboven, P., Verlinden, B., Schenk, A., Nicolai, B. (2013c). Controlled atmosphere storage may lead to local ATP deficiency in apple. *Postharvest Biology and Technology*, 78, 103-112.

Hoa, T., Ducamf, M., Lebrup, M., & Baldwin, E. (2002). Effect of different coating treatments on the quality of mango fruit. *Journal of Food Quality*, 25, 471-486.

Kuroki, S., Oshita, S., Sotome, I., Kawagoe, Y., & Seo, Y. (2004). Visualization of 3-D network of gas-filled intercellular spaces in cucumber fruit after harvest. *Postharvest Biology Technology*, 33, 255-262.

Lammertyn, J., Dresselaers, T., Van Hecke, P., Jancsok, P., Wevers, M., & Nicolaı, B.M. (2003a). Analysis of the time course of core breakdown in 'Conference' pears by means of MRI and X-ray CT. *Postharvest Biology and Technology*, 29, 19-28.

Lammertyn, J., Dresselaers, T., Van Hecke, P., Jancsok, P., Wevers, M., & Nicolai, B.M. (2003b). MRI and X-ray CT study of spatial distribution of core breakdown in 'Conference' pears. *Magnetic Resonance Imaging*, 21, 805–815.

Lizada, C. (1993). Mango. In G.B. Seymour, J.E. Taylor, & G.A. Tucker (Eds.), *Biochemistry of Fruit Ripening* (pp. 225–271). London: Chapman and Hall.

Mebatsion, H.K., Verboven, P., Ho, Q.T., Verlinden, B.E., & Nicolai, B.M. (2008). Modelling fruit (micro)structures, why and how?. *Trends in Food Science and Technology*, 19, 59-66.

Mendoza, F., Verboven, P., Mebatsion, H.K., Kerckhofs, G., Wevers, M., & Nicolai, B. (2007). Three-dimensional pore space quantification of apple tissue using X-ray computed microtomography. *Planta*, 226, 559-570.

Meyer, F., & Beucher, S. (1990). Morphological segmentation. *Journal of Visual Communication and Image Representation*, 1, 21–46.

Mohammed, M., & Brecht, J.K. (2002). Reduction of chilling injury in 'Tommy Atkins' mangoes during ripening. *Scientia Horticulturae*, 95, 297–308.

Odgaard, A. (1997). Three-dimensional methods for quantification of cancellous bone architecture. *Bone*, 20, 315-328.

Parikh, H.R., Nair, G.M., & Modi, V.V. (1990). Some structural changes during ripening of mangoes (*Mangifera indica* var. Alphonso) by abscisic acid treatment. *Annals of Botany*, 65, 121–127.

Selvaraj, Y., Kumar, R., & Pal, D.K. (1989). Changes in sugars, organics acids, amino acids, lipid constituents and aroma characteristics of ripening mango (*Mangifera indica* L.) fruit. *Journal of Food Science and Technology*, 26, 306–311.

Singh, Z., Singh, R.K., Sane, V.A., & Nath, P. (2013). Mango – Postharvest biology and biotechnology. *Critical Reviews in Plant Sciences*, 32(4), 217-236.

Suzuki, K. (1993). Aging and biomembranes in plants. *Research Journal in Food and Agriculture*, 16, 23-27.

Verboven, P., Kerckhofs, G., Mebatsion, H.K., Ho, Q., Temst, K., Wevers, M., et al. (2008). Three-dimensional gas exchange pathways in pome fruit characterized by synchrotron X-ray computed tomography. *Plant Physiology*, 147, 518-527.

Volz, R.K., Harker, F.R., Hallet, I.C., & Lang, A. (2004). Development of Texture in Apple Fruit – a Biophysical Perspective. *Acta Horticulturae*, 636, 473–479.

Voragen, A. G. J., Pilnik, W., Thibault, J. F., Axelos, M. A.V., & Renard, C. M. C. G. (1995). Pectins. In A.M. Stephen (Ed.) *Food Polysaccharides and their Applications* (pp. 287–339). New York: Marcel Dekker Inc.

Yaptenco, K.F., Lacao, M.A.J., Esguerra, E.B., & Serrano, E.P. (2010). Optimization and pilot scale testing of modified atmosphere packaging of irradiated fresh 'Carabao' Mango (*Mangifera indica L.*) fruits. *Philippine Journal of Crop Science*, 35(2), 23-33.

8 Tables

Table 1. Morphometric parameters and description used to quantify the microstructure.

Microstructural parameter	**Unit**	**Description**
Cell specific surface area	mm^{-1}	Surface area of individual mesocarp cell divided by the cell volume
Cell surface area	mm^2	Area of individual mesocarp cell surface
Euler number	(-)	Indicator of connectedness of a 3-D complex structure, and a global characterization of topology. Higher values indicate poorly connected structures and lower values for better connected structures (Gunderson, Boyce, Nyengaard, & Odgaard, 1993).
Feret diameter	mm	Measure of an object size along a specified direction.
Fragmentation index	mm^{-1}	Inverse index of connectivity, calculated by comparing volume and surface of the binarised object before and after an image dilation (Hahn, Vogel, Pompesius-Kempa, & Delling, 1992). A lower fragmentation signifies better connected structures.
Length	mm	Maximum of Feret diameters measured over a range of angles
Pore specific surface area	mm^{-1}	Surface area of the interface between tissue and gas-filled intercellular space divided by the volume of the gas-filled intercellular space

Pore structure thickness	mm	Average of the local thickness of the pores. Calculated by skeletonisation of the binarised tissue, followed by a sphere fitting algorithm for each voxel of the skeleton (Hildebrand & Ruegsegger, 1997).
Porosity	%	Pore volume divided by total volume of the analyzed sample (tissue and pores)
Structural anisotropy	(-)	Measure of 3-D symmetry or the presence or absence of preferential alignment of structures along a particular directional axis. This value is scaled from 0 for total isotropy to 1 for total anisotropy (Odgaard, 1997) .
Tissue specific surface area	mm^{-1}	Surface area of tissue or aggregates of mesocarp cells divided by its volume
Tissue thickness	mm	Average of the local thickness of the tissue space. Calculated by a skeletonisation of the binarised tissue, followed by a sphere fitting algorithm for each voxel of the skeleton (Hildebrand & Ruegsegger, 1997).
Volume	mm^3	Total volume of the sample (tissue and pores)
Width	mm	Minimum of Feret diameters measured over a range of angles

(Herremans et al., 2013, with modifications)

Table 2. Three-dimensional morphometric parameters of individual cells derived from manually segmenting cells of unripe mango. Mean values are presented with their standard error (n = 60). Means followed by different letters are significantly different at 0.05 level of significance.

Morphometric parameters	Outer mesocarp	Inner mesocarp
Cell volume (mm^3)	0.001161 ± 0.000046 (A)	0.000813 ± 0.000024 (B)
Cell surface area (mm^2)	0.0560 ± 0.0015 (A)	0.04399 ± 0.00087 (B)
Cell specific surface area (mm^{-1})	49.74 ± 0.70 (B)	55.06 ± 0.58 (A)
Cell length (mm)	0.1601 ± 0.0022 (A)	0.1424 ± 0.0017 (B)
Cell width (mm)	0.1090 ± 0.0020 (A)	0.1008 ± 0.0015 (B)
Cell length/width	1.485 ± 0.023	1.425 ± 0.018
Sphericity	0.9452 ± 0.0026	0.9526 ± 0.0026

Table 3. Three-dimensional morphometric parameters of individual cells derived from watershed segmentation of cells from unripe mango. Mean values are presented with their standard error (n = 800). Means followed by different letters are significantly different at 0.05 level of significance.

Morphometric parameters	Outer mesocarp	Inner mesocarp
Cell volume (mm^3)	$9355 \times 10^{-7} \pm 90 \times 10^{-7}$ (A)	$7152 \times 10^{-7} \pm 68 \times 10^{-7}$ (B)
Cell surface area (mm^2)	0.05285 ± 0.00032 (A)	0.04341 ± 0.00028 (B)
Cell specific surface area (mm^{-1})	57.94 ± 0.21 (B)	62.30 ± 0.23 (A)
Cell length (mm)	0.16431 ± 0.00056 (A)	0.14618 ± 0.00047 (B)
Cell width (mm)	0.10646 ± 0.00045 (A)	0.10227 ± 0.00039 (B)
Cell length/width	1.5548 ± 0.0055 (A)	1.4363 ± 0.0041 (B)
Sphericity	0.8687 ± 0.0013 (B)	0.8845 ± 0.0011 (A)

Table 4. Sphericity of individual cells and pores in outer mesocarp of mango samples during ripening at 20°C. Individual cells were derived from automatic cell segmentation procedure. Mean values are presented with their standard error. Means followed by different letters are significantly different at 0.05 level of significance.

	Days at storage	
	0	9
n		
Cells	800	633
Pores	4437	9638
Sphericity		
Cells	0.8687 ± 0.0013 (A)	0.7553 ± 0.0017 (B)
Pores	0.3298 ± 0.0065 (B)	0.3616 ± 0.0043 (A)
Pores (Volume weighted)	0.30343 ± 0.00062 (B)	0.50879 ± 0.00042 (A)

Table 5. Morphometric parameters for outer and inner mesocarp samples of mangoes during ripening at 20°C. Also given are statistics of the pore space distribution. Mean values are presented with their 95% confidence interval.

	Days at storage			
	0	3	6	9
n				
Outer mesocarp	12	12	12	8
Inner mesocarp	12	12	12	8
Porosity (%)				
Outer mesocarp	14.26 ± 0.94	13.6 ± 1.8	9.1 ± 1.6	11.7 ± 1.7
Inner mesocarp	12.3 ± 1.0	12.2 ± 1.3	8.9 ± 1.4	8.4 ± 2.9
Pore specific surface area (mm^{-1})				
Outer mesocarp	191.1 ± 7.0	199.5 ± 5.0	210.9 ± 10.4	221.7 ± 7.0
Inner mesocarp	206.0 ± 7.3	209.4 ± 6.6	221.5 ± 13.3	233 ± 18
Pore fragmentation (mm^{-1})				
Outer mesocarp	68.1 ± 3.0	76.2 ± 6.6	85.5 ± 8.2	81.4 ± 6.8
Inner mesocarp	79.4 ± 4.3	79.5 ± 3.4	89.9 ± 6.6	88 ± 12
Pore structure thickness (mm)				
Outer mesocarp	0.02571 ± 0.00060	0.02490 ± .00050	0.02420 ± 0.00077	0.02307 ± 0.00034
Inner mesocarp	0.02476 ± 0.00077	0.02427 ± .00092	0.02349 ± 0.0010	0.02154 ± 0.00088
Pore anisotropy				
Outer mesocarp	0.300 ± 0.020	0.296 ± 0.012	0.348 ± 0.055	0.397 ± 0.012
Inner mesocarp	0.390 ± 0.050	0.351 ± 0.063	0.414 ± 0.035	0.450 ± 0.039
Pore connectivity				
Outer mesocarp	$508 \times 10^2 \pm 68 \times 10^2$	$42 \times 10^3 \pm 16 \times 10^3$	$204 \times 10^2 \pm 82 \times 10^2$	$32 \times 10^3 \pm 13 \times 10^3$
Inner mesocarp	$383 \times 10^2 \pm 84 \times 10^2$	$42 \times 10^3 \pm 12 \times 10^3$	$176 \times 10^2 \pm 59 \times 10^2$	$22 \times 10^3 \pm 20 \times 10^3$
Tissue specific surface area (mm^{-1})				

Outer mesocarp	32.4 ± 2.5	34.2 ± 4.2	22.9 ± 3.2	28.5 ± 3.0
Inner mesocarp	30.4 ± 1.8	30.3 ± 1.7	23.2 ± 2.4	23.9 ± 7.3
Tissue thickness (mm)				
Outer mesocarp	0.0677 ± 0.0022	0.0716 ± 0.0067	0.091 ± 0.012	0.0750 ± 0.0074
Inner mesocarp	0.0690 ± 0.0034	0.0660 ± 0.0027	0.0783 ± 0.0034	0.078 ± 0.016
Tissue anisotropy				
Outer mesocarp	0.268 ± 0.022	0.275 ± 0.019	0.312 ± 0.049	0.3693 ± 0.019
Inner mesocarp	0.350 ± 0.020	1.369 ± 0.022	0.3842 ± 0.032	0.4203 ± 0.026
Euler number				
Outer mesocarp	$-205 \times 10^2 \pm 73 \times 10^2$	$-119 \times 10^2 \pm 66 \times 10^2$	$12 \times 10^3 \pm 13 \times 10^3$	$105 \times 10^2 \pm 50 \times 10^2$
Inner mesocarp	$1 \times 10^3 \pm 12 \times 10^3$	$7 \times 10^3 \pm 12 \times 10^3$	$289 \times 10^2 \pm 77 \times 10^2$	$294 \times 10^2 \pm 74 \times 10^2$
Skewness of pore space distribution				
Outer mesocarp	168.5 ± 9.6	168.6 ± 7.8	181 ± 21	196 ± 22
Inner mesocarp	184.1 ± 9.9	183.8 ± 12.6	178 ± 27	188 ± 27
Kurtosis of individual pore space distribution				
Outer mesocarp	$275 \times 10^2 \pm 21 \times 10^2$	$286 \times 10^2 \pm 26 \times 10^2$	$338 \times 10^2 \pm 76 \times 10^2$	$391 \times 10^2 \pm 87 \times 10^2$
Inner mesocarp	$344 \times 10^2 \pm 39 \times 10^2$	$342 \times 10^2 \pm 46 \times 10^2$	$323 \times 10^2 \pm 90 \times 10^2$	$32 \times 10^3 \pm 17 \times 10^3$
Maximal individual pore volume (mm^3)				
Outer mesocarp	$823 \times 10^{-5} \pm 62 \times 10^{-5}$	$37 \times 10^{-5} \pm 26 \times 10^{-5}$	$11.9 \times 10^{-5} \pm 7.2 \times 10^{-5}$	$13.1 \times 10^{-5} \pm 9.2 \times 10^{-5}$
Inner mesocarp	$31 \times 10^{-5} \pm 20 \times 10^{-5}$	$21 \times 10^{-5} \pm 12 \times 10^{-5}$	$6.3 \times 10^{-5} \pm 1.2 \times 10^{-5}$	$5.0 \times 10^{-5} \pm 2.0 \times 10^{-5}$

9 Figure Captions

Figure 1. Excision of mango samples at the fruit equator for Micro-CT (a) and subdivision of the tissue sample as outer and inner mesocarp based on the radial distance, R in the fruit (b). Cropping of the sides (1 mm) and the top and bottom portion (1.25 mm) of the sample to ensure intact and undamaged samples for analysis (c). The final volume left for analysis was 24 mm^3.

Figure 2. Micro-CT cross section before (a) and after (b) binarization by Otsu thresholding and typical grayscale histogram for the unripe and ripe fruit (c). The selection of a global threshold (indicated by the arrow at threshold value of 63) based on Otsu's algorithm was used to maximize the 'between-class variance' giving the best separation of tissue and pores (d). Scale bar measures 500 µm.

Figure 3. Representative elementary volume analysis, showing porosity for different volume sizes (a) and their corresponding standard deviation (b) using 4 individual fruit samples. Mean and Standard deviation followed by the same letters are not significantly different. Error bars represent 95% confidence limits (n = 12).

Figure 4. Automatic watershed segmentation showing sample volume in grayscale (a) and the resulting watershed separation lines (b). Surface rendering of individual cells in outer (a) and inner (b) mesocarp based on manual segmentation and watershed procedures shown alongside with the 3 orthogonal views in the background. Sixty cells of outer and inner mesocarp were manually segmented. These manually segmented cells showed close grouping with most of the cells in contact with each other. Watershed segmented cells (754 in outer mesocarp and 820 for

inner mesocarp) were shown after filtering broken cells and unseparated cluster of cells prior to analysis. Side length of cubes measures 1.5 mm.

Figure 5. Automatic watershed segmentation of unripe and ripe outer mesocarp showing the sample volume in grayscale (a), 3-D model of the same sample after the automatic cell segmentation procedure (b), and surface rendering of the isolated cells (c) and pores (d). Colors identify individual cells and pores. Side length of cubes measures 1.5 mm, except for pores (d) where side length measures 0.25 mm.

Figure 6. Manual segmentation of unripe and ripe mesocarp cells showing changes in cell shape during ripening and the possible occurrence of cell leakage, indicated by the blue segmented region connecting cells after ripening for 9 days at 20°C.

Figure 7. Pore network of outer mesocarp of mango stored at 20°C: (a) reconstructed X-ray CT slices, (b) 3-D geometric models of tissue and (c) 3-D pore network model showing the essential geometry, branching, as well as local thickness (in color bar) of pores. Scale bar and side length of cubes measures 500 µm.

Figure 8. Pore network of inner mesocarp of mango stored at 20°C: (a) reconstructed X-ray CT slices, (b) 3-D geometric models of tissue and (c) 3-D pore network model showing the essential geometry, branching, as well as local thickness (in color bar) of pores. Scale bar and side length of cubes measures 500 µm.

Figure 9. Pore space distribution expressed as cumulative volume (A) and volume of pore fraction (B) as a function of pore equivalent diameter (mm) for unripe outer and inner mesocarp and ripe outer and inner mesocarp. Error bars represent 95 % confidence of the mean of 5 samples.

Figure 10. Plot of 3-D structural parameters in outer (♦) and inner (■) mesocarp of mango during ripening at 20°C. Error bars indicate 95% confidence of the mean (n = 12).

Figure 11. PLS-DA bi-plot showing morphometric parameter loadings (×) and unripe (closed symbols) and ripe (open symbols) samples from different sampling positions (inner (□) and outer (△) mesocarp). The percentage explained variance is indicated on the axes. Only the most important variables, situated between 70 and 100% explained variance limits are named. These variables have the highest discriminating ability for separating each class. The response vector indicated in arrows, show the direction of discrimination between ripe and unripe, and inner and outer mesocarp samples.

10 Figures

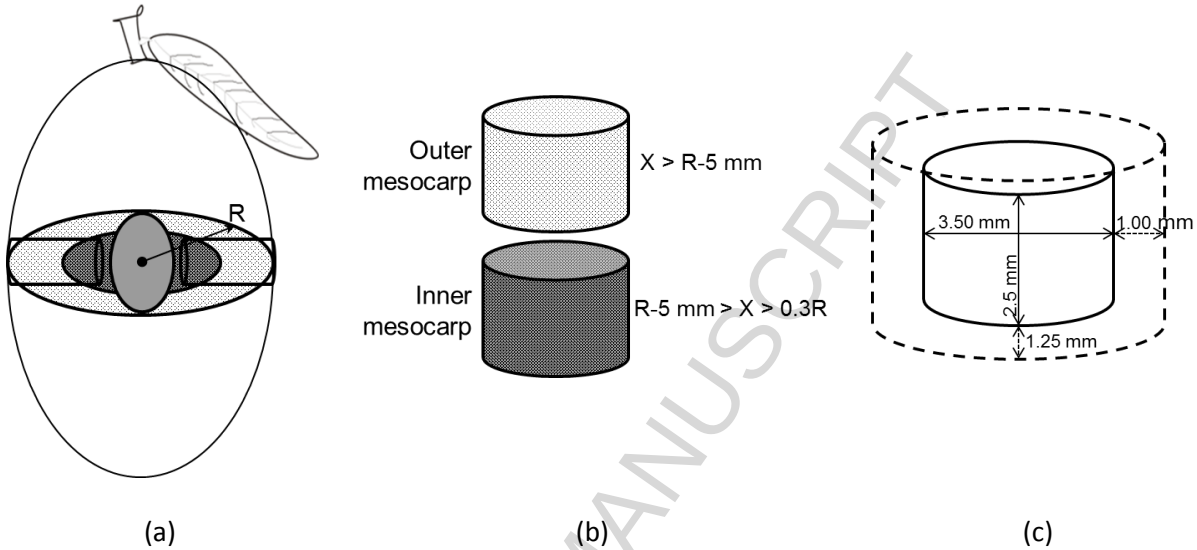

Figure 1. Excision of mango samples at the fruit equator for Micro-CT (a) and subdivision of the tissue sample as outer and inner mesocarp based on the radial distance, R in the fruit (b). Cropping of the sides (1 mm) and the top and bottom portion (1.25 mm) of the sample to ensure intact and undamaged samples for analysis (c). The final volume left for analysis was 24 mm^3.

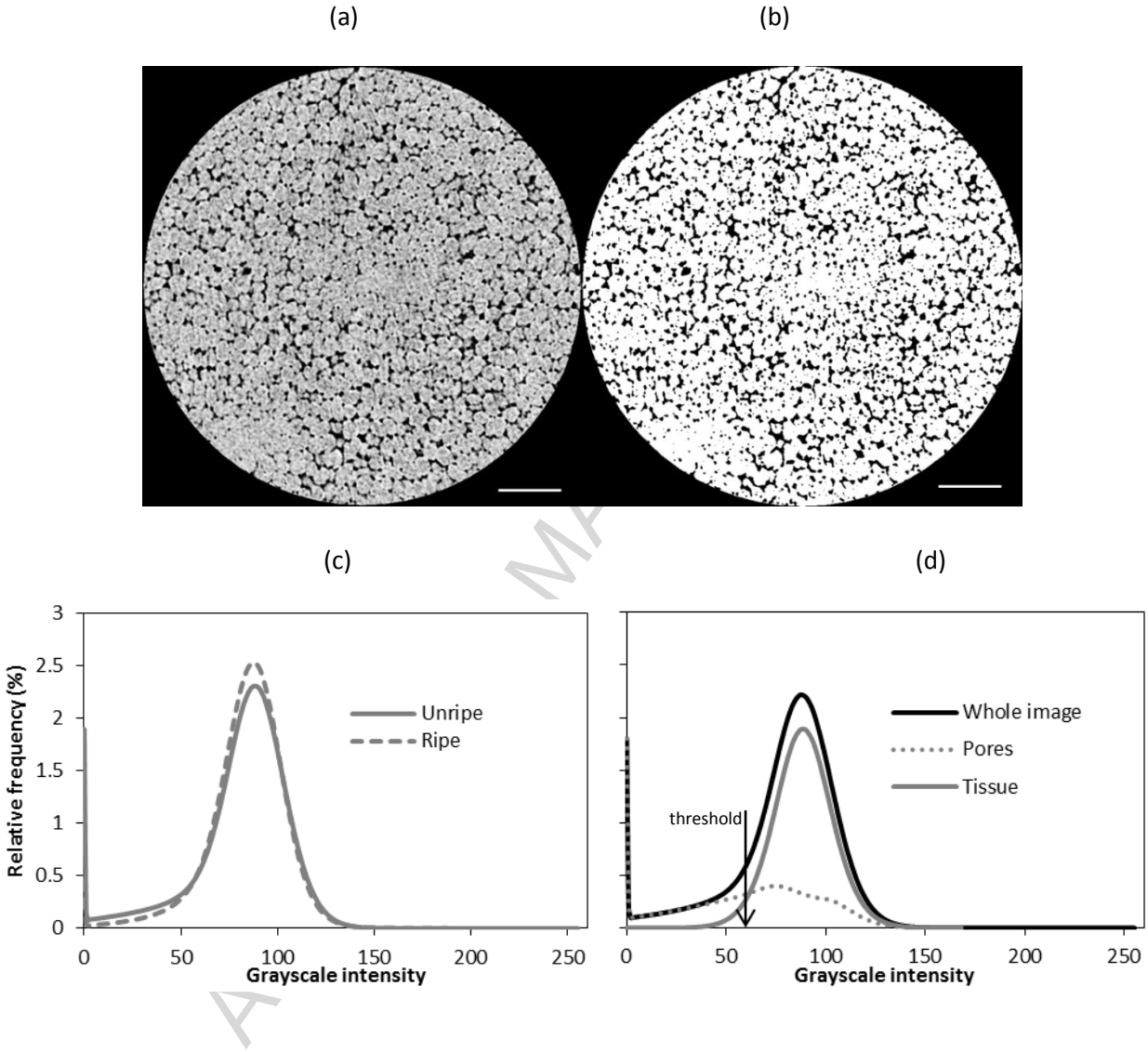

Figure 2. Micro-CT cross section before (a) and after (b) binarization by Otsu thresholding and typical grayscale histogram for the unripe and ripe fruit (c). The selection of a global threshold (indicated by the arrow at threshold value of 63) based on Otsu's algorithm was used to maximize the 'between-class variance' giving the best separation of tissue and pores (d). Scale bar measures 500 µm.

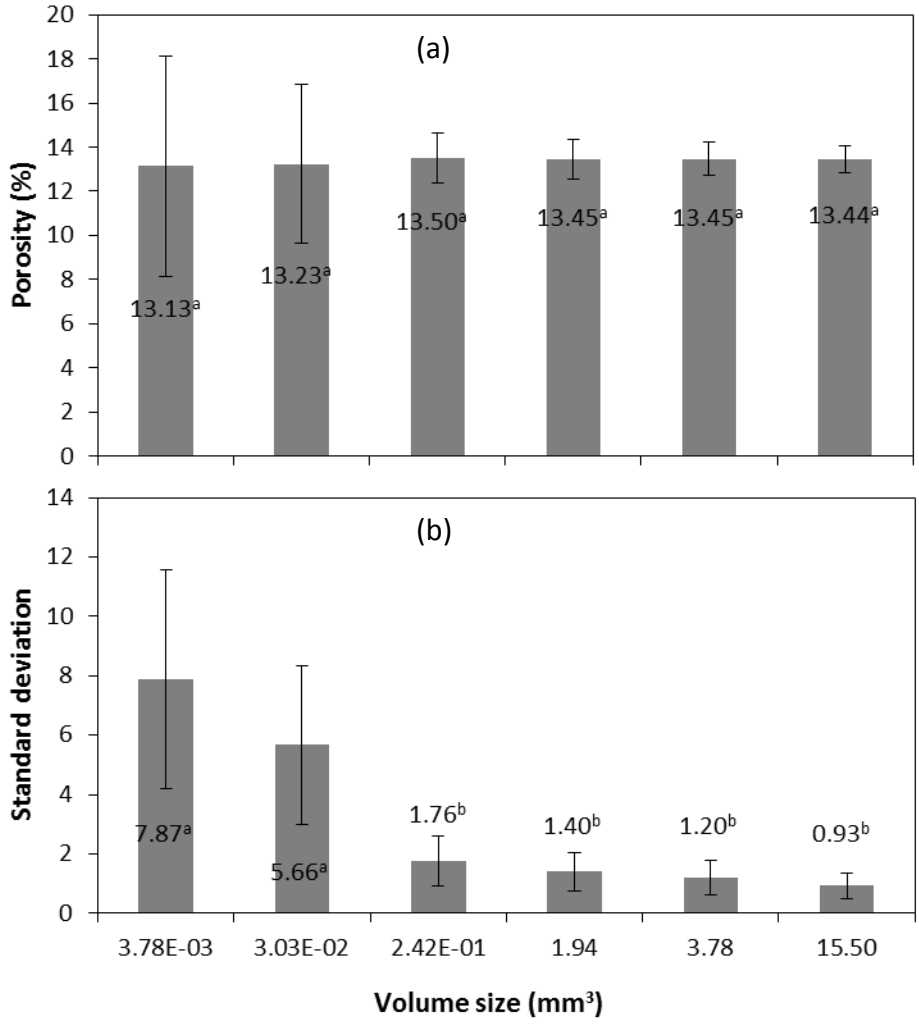

Figure 3. Representative elementary volume analysis, showing porosity for different volume sizes (a) and their corresponding standard deviation (b) using 4 individual fruit samples. Mean and Standard deviation followed by the same letters are not significantly different. Error bars represents 95% confidence limits (n = 12).

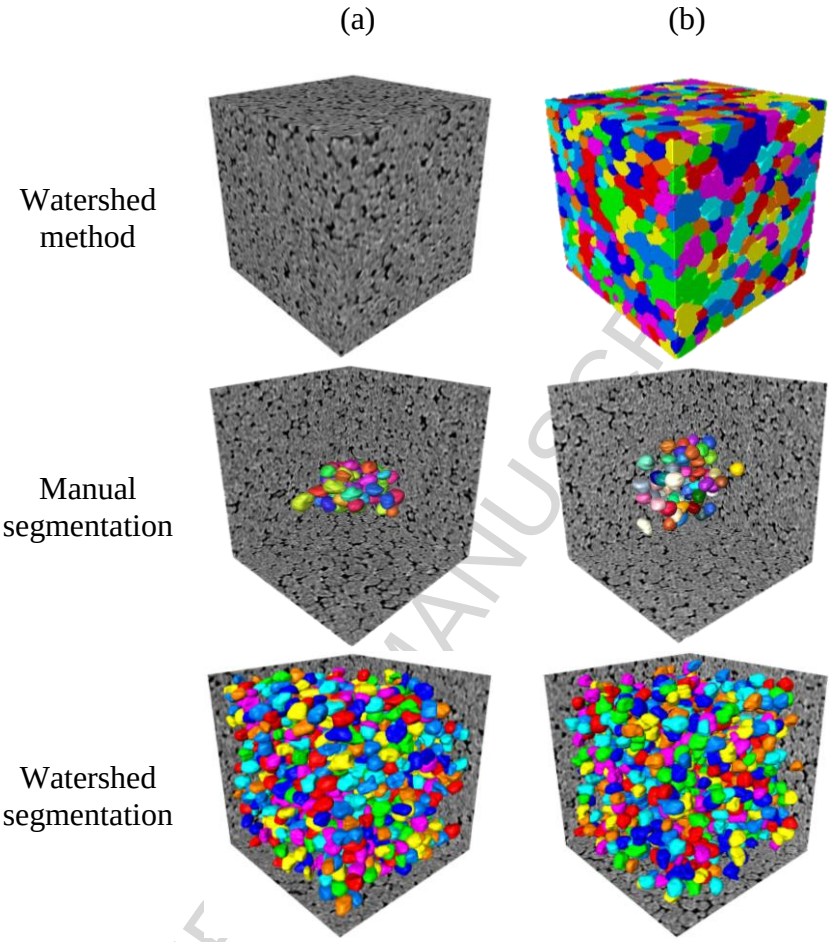

Figure 4. Automatic watershed segmentation showing sample volume in grayscale (a) and the resulting watershed separation lines (b). Surface rendering of individual cells in outer (a) and inner (b) mesocarp based on manual segmentation and watershed procedures shown alongside with the 3 orthogonal views in the background. Sixty cells of outer and inner mesocarp were manually segmented. These manually segmented cells showed close grouping with most of the cells in contact with each other. Watershed segmented cells (754 in outer mesocarp and 820 for inner mesocarp) were shown after filtering broken cells and unseparated cluster of cells prior to analysis. Side length of cubes measures 1.5 mm.

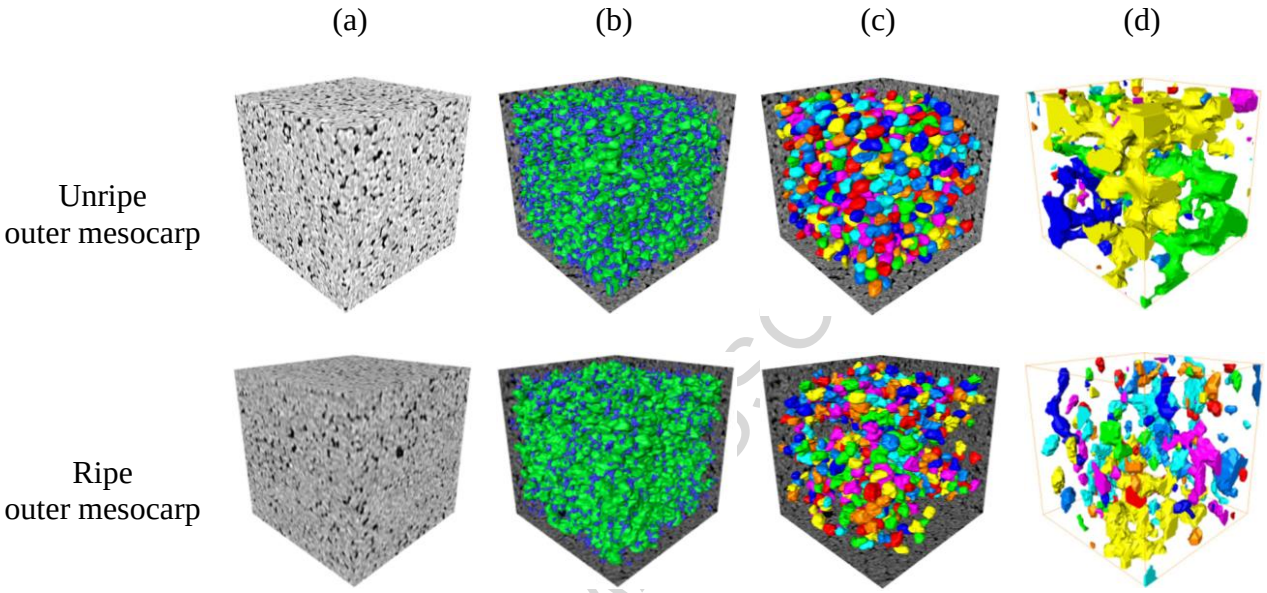

Figure 5. Automatic watershed segmentation of unripe and ripe outer mesocarp showing the sample volume in grayscale (a), 3-D model of the same sample after the automatic cell segmentation procedure (b), and surface rendering of the isolated cells (c) and pores (d). Colors identify individual cells and pores. Side length of cubes measures 1.5 mm, except for pores (d) where side length measures 0.25 mm.

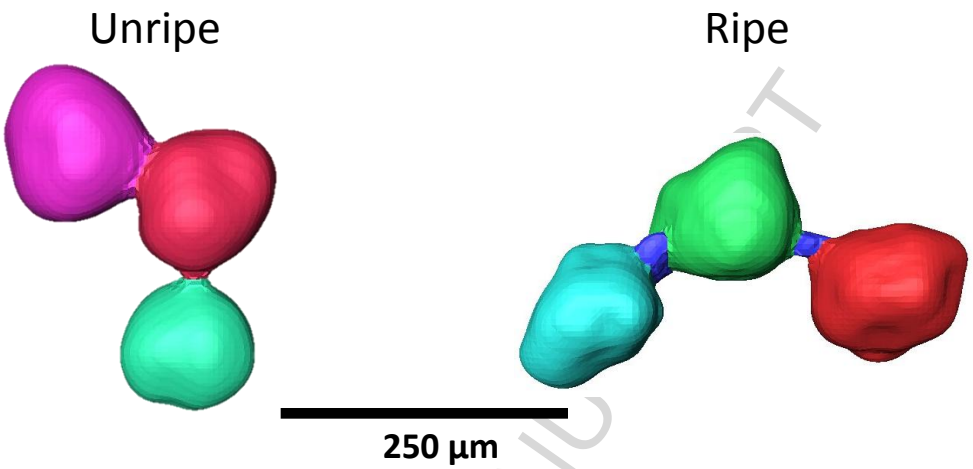

Figure 6. Manual segmentation of unripe and ripe mesocarp cells showing changes in cell shape during ripening and the possible occurrence of cell leakage, indicated by the blue segmented region connecting cells after ripening for 9 days at 20°C.

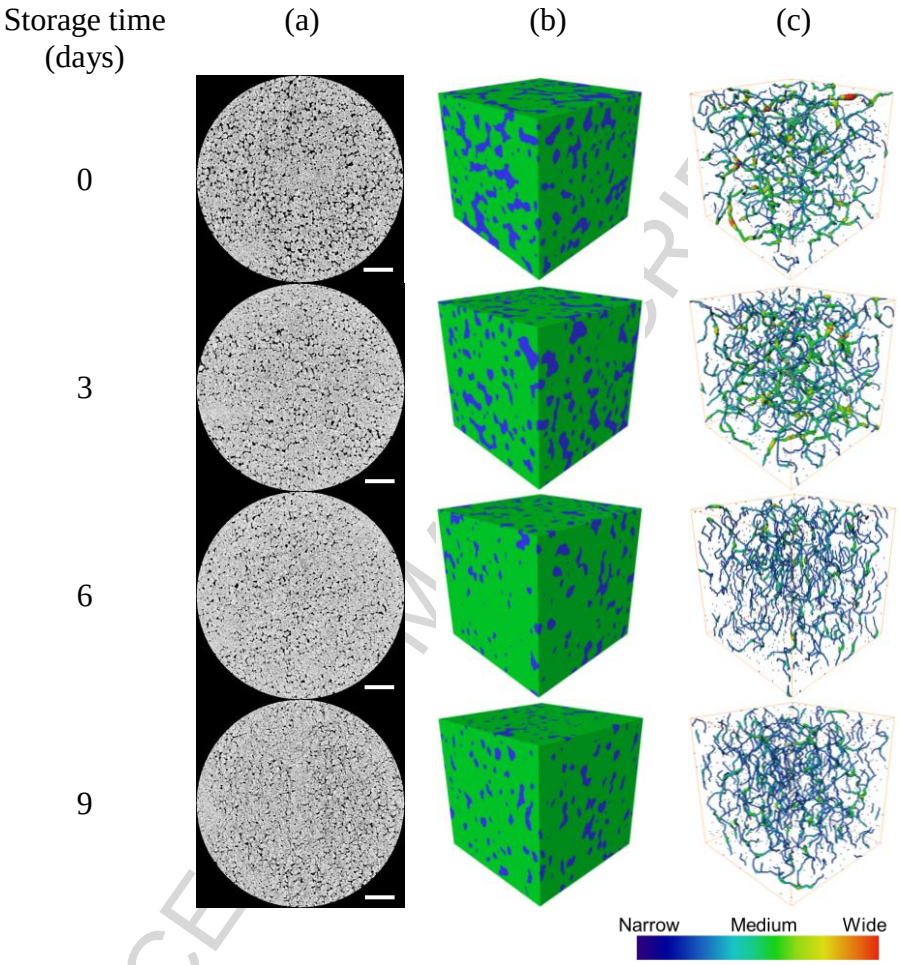

Figure 7. Pore network of outer mesocarp of mango stored at 20°C: (a) reconstructed X-ray CT slices, (b) 3-D geometric models of tissue, and (c) 3-D pore network model showing the essential geometry, branching, as well as local thickness (in color bar) of pores. Scale bar and side length of cubes measures 500 µm.

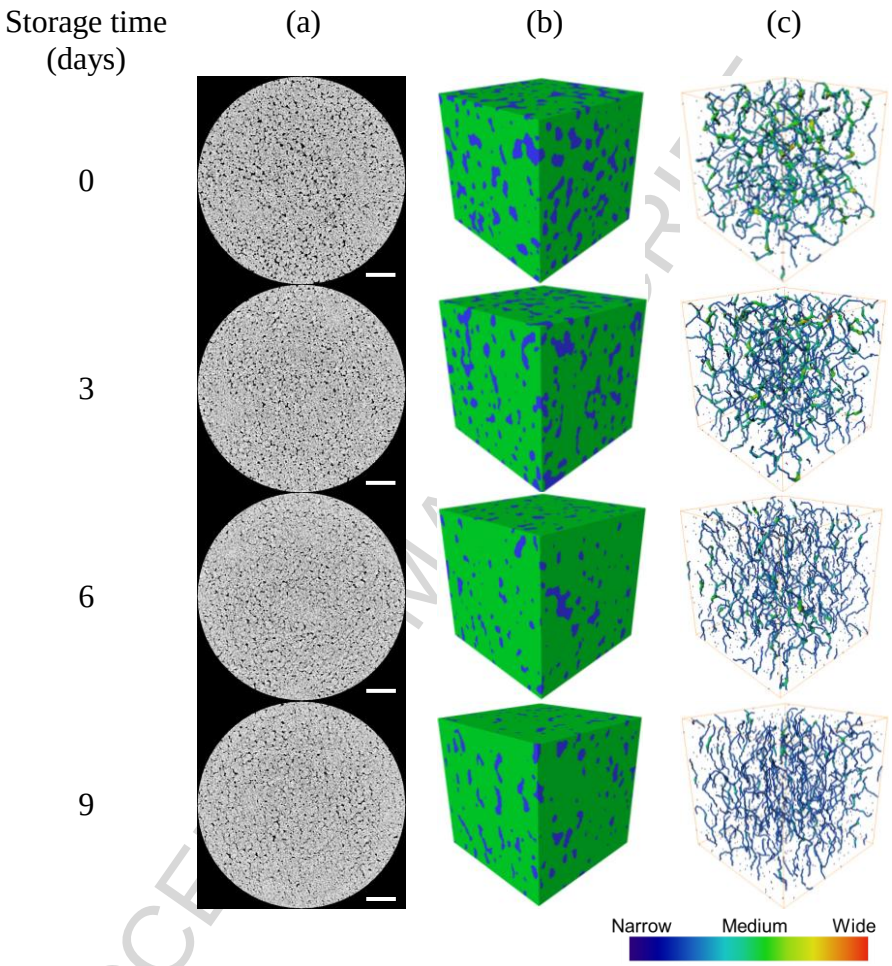

Figure 8. Pore network of inner mesocarp of mango stored at 20°C: (a) reconstructed X-ray CT slices, (b) 3-D geometric models of tissue, and (c) 3-D pore network model showing the essential geometry, branching, as well as local thickness (in color bar) of pores. Scale bar and side length of cubes measures 500 µm.

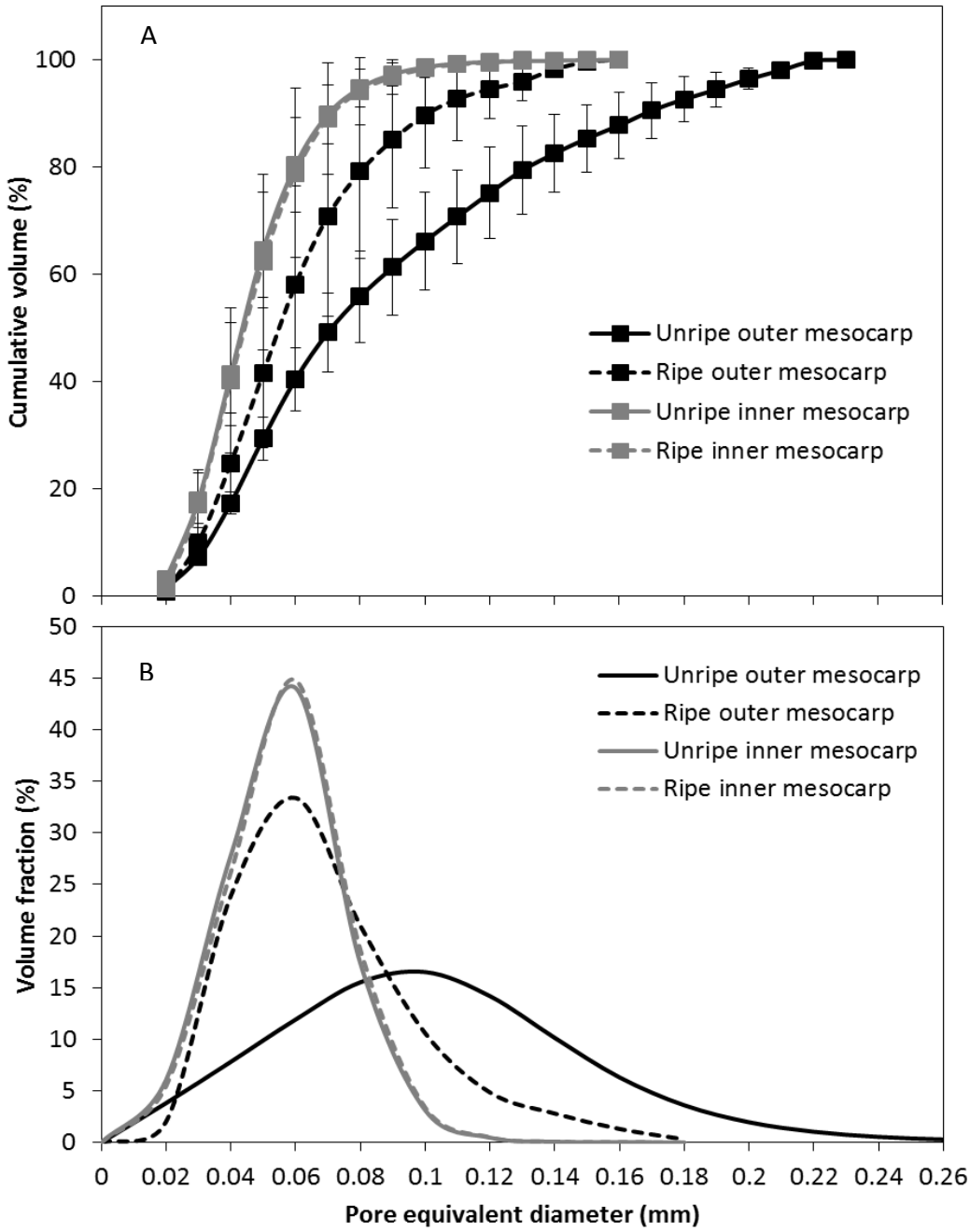

Figure 9. Pore space distribution expressed as cumulative volume (A) and volume of pore fraction (B) as a function of pore equivalent diameter (mm) for unripe outer and inner mesocarp and ripe outer and inner mesocarp. Error bars represent 95 % confidence of the mean of 5 samples.

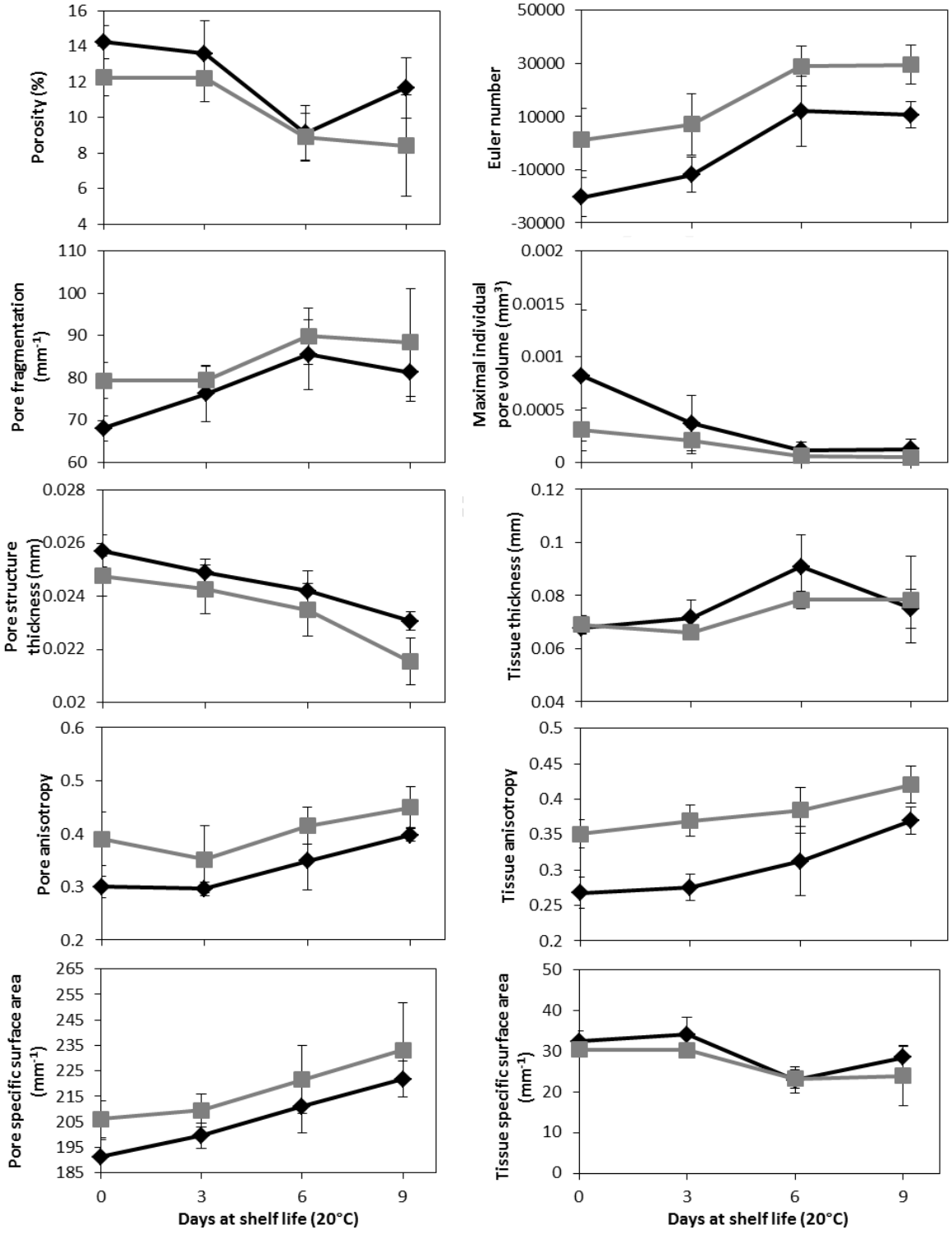

Figure 10. Plot of 3-D microstructural parameters in outer (♦) and inner (■) mesocarp of mango during ripening at 20°C. Error bars indicate 95% confidence of the mean (n = 12).

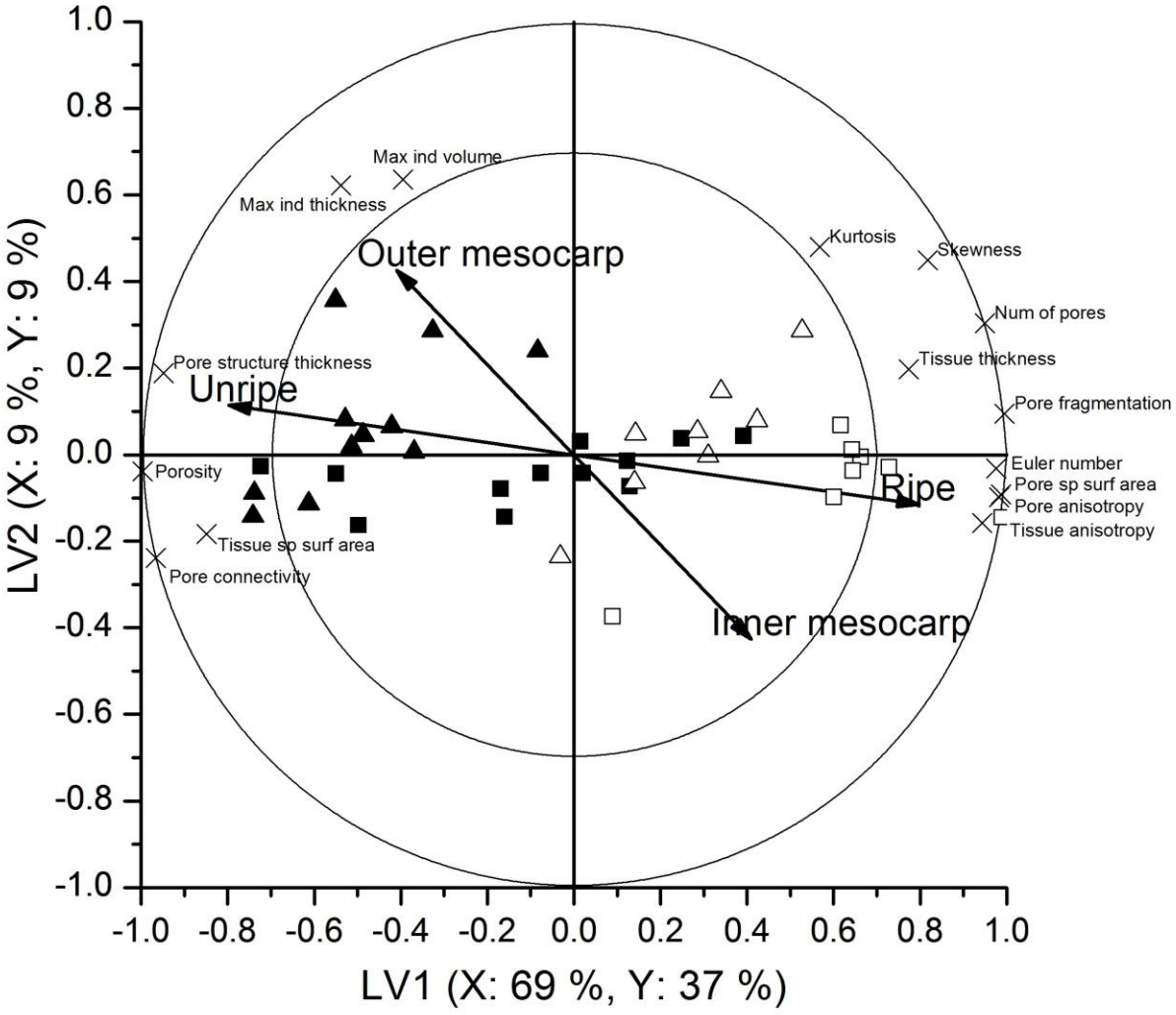

Figure 11. PLS-DA bi-plot showing morphometric parameter loadings (×) and unripe (closed symbols) and ripe (open symbols) samples from different sampling positions (inner (□) and outer (△) mesocarp). The percentage explained variance is indicated on the axes. Only the most important variables, situated between 70 and 100% explained variance limits are named. These variables have the highest discriminating ability for separating each class. The response vector indicated in arrows, show the direction of discrimination between ripe and unripe, and inner and outer mesocarp samples.